Low-bandgap mixed tin–lead iodide perovskite absorbers with long carrier lifetimes for all-perovskite tandem solar cells

Dewei Zhao[1*†], Yue Yu[1†], Changlei Wang[1,2†], Weiqiang Liao[1,3†], Niraj Shrestha[1], Corey R. Grice[1], Alexander J. Cimaroli[1], Lei Guan[1], Randy J. Ellingson[1], Kai Zhu[4], Xingzhong Zhao[2], Ren-Gen Xiong[3] and Yanfa Yan[1*]

Tandem solar cells using only metal-halide perovskite sub-cells are an attractive choice for next-generation solar cells. However, the progress in developing efficient all-perovskite tandem solar cells has been hindered by the lack of high-performance low-bandgap perovskite solar cells. Here, we report efficient mixed tin–lead iodide low-bandgap (∼1.25 eV) perovskite solar cells with open-circuit voltages up to 0.85 V and over 70% external quantum efficiencies in the infrared wavelength range of 700–900 nm, delivering a short-circuit current density of over 29 mA cm^{-2} and demonstrating suitability for bottom-cell applications in all-perovskite tandem solar cells. Our low-bandgap perovskite solar cells achieve a maximum power conversion efficiency of 17.6% and a certified efficiency of 17.01% with a negligible current–voltage hysteresis. When mechanically stacked with a ∼1.58 eV bandgap perovskite top cell, our best all-perovskite 4-terminal tandem solar cell shows a steady-state efficiency of 21.0%.

Organic–inorganic metal-halide perovskites have been attracting much attention as promising photovoltaic materials in recent years due to their unique photovoltaic properties[1–5]. The power conversion efficiency (PCE) of perovskite solar cells (PVSCs) has been remarkably boosted from 3.8% to a certified 22.1% (refs 6–9). A proven concept for further improving the efficiency of PVSCs beyond the Shockley–Queisser limit for single-junction solar cells is to fabricate tandem solar cells, which consist of a wide-bandgap top cell and a low-bandgap bottom cell. Device modelling has shown that for efficient two-junction monolithic tandem cells, the top cell should have a bandgap of ∼1.7–1.9 eV, whereas the bottom cell should have a bandgap of ∼0.9–1.2 eV (refs 10–12). Lead (Pb) and tin (Sn) halide perovskites exhibit excellent bandgap tunability. Pb mixed iodide (I) and bromine (Br) perovskites cover the bandgap range of 1.58 (pure I) to 2.20 eV (pure Br)[1], while mixed Sn and Pb iodide perovskites exhibit bandgaps from 1.17 (50% Sn and 50% Pb) to 1.58 eV (pure Pb)[13–16], making them suitable for the top- and bottom-cell application in tandem solar cells, respectively. Additionally, the low-temperature processing used for both wide- and low-bandgap metal-halide perovskites avoids undesirable damage, making the fabrication of all-perovskite tandem cells feasible.

Fabricating efficient all-metal-halide perovskite tandem solar cells requires the development of both wide- and low-bandgap PVSCs with efficient performance and high open-circuit voltages (V_{oc}) with respect to their absorber layer bandgaps. However, the progress in developing high-V_{oc} and efficient wide-bandgap PVSCs is far ahead of developing efficient low-bandgap PVSCs.

For example, using mixed formamidinium (FA) and caesium (Cs) cations and mixed halide Pb perovskites, Snaith and co-workers have demonstrated a wide-bandgap (1.74 eV) PVSC with a PCE of 17% and a V_{oc} of 1.2 V (ref. 1). The low-bandgap perovskite solar cells reported in the literature showed much lower PCEs[13,17–21]. Jen and co-workers reported MASn$_x$Pb$_{1-x}$I$_{3-x}$Cl$_x$ (MA = methylammonium, Cl = chlorine, x varies from 1 to 3) PVSCs[19,20], but the PCE is only 10% and 14.2% for 1.38 eV and 1.33 eV bandgap PVSCs[18], respectively. MASn$_{0.5}$Pb$_{0.5}$I$_3$ has a bandgap of 1.17 eV (refs 13,17). Li et al. reported a PCE of up to 13.6% from MASn$_{0.5}$Pb$_{0.5}$I$_3$-based PVSCs[21]. Recently, by mixing FASnI$_3$ and MAPbI$_3$ precursors, we have successfully fabricated 15.0% PVSCs with a bandgap of ∼1.25 eV (ref. 16). Even more recently, McGehee and Snaith and co-workers have successfully demonstrated efficient all-perovskite 2-terminal tandem cells consisting of 1.8 eV wide-bandgap FA$_{0.83}$Cs$_{0.17}$Pb(I$_{0.5}$Br$_{0.5}$)$_3$ top cells and 1.22 eV low-bandgap FA$_{0.75}$Cs$_{0.25}$Sn$_{0.5}$Pb$_{0.5}$I$_3$ bottom cells[10]. Their best low-bandgap cell produces a PCE of 14.8% with a V_{oc} of 0.74 V. Their best 4-terminal tandem cell produces an impressive PCE of 20.3% (ref. 10). All reported low-bandgap PVSCs show relatively low spectral response in the near infrared (IR) wavelength range beyond 700 nm, which includes the light passing through the top cell, rendering them non-ideal for the bottom cell in tandem solar cells. Therefore, many research efforts on efficient tandem cells have been focused on combining wide-bandgap PVSCs with Si[1,22–24], copper indium gallium diselenide[25–27] and polymer-based low-bandgap bottom cells[28]. Compared with these tandem cells, the all-perovskite ones could be manufactured at lower costs due to the low-temperature processing and the ease of fabrication.

Here, we report low-bandgap ($\sim$1.25 eV) single-junction mixed Sn–Pb PVSCs with a maximum PCE of 17.6% and a certified PCE of 17.01%, which are as high as that of the best wide-bandgap $FA_{0.83}Cs_{0.17}Pb(I_{0.6}Br_{0.4})_3$ PVSCs[4]. More importantly, our low-bandgap PVSCs show V_{oc} up to 0.85 V. Furthermore, our low-bandgap PVSCs show external quantum efficiency (EQE) of more than 70% in the IR wavelength range of 700 to 900 nm, leading to a record short-circuit current density (J_{sc}) of over 29 mA cm^{-2} for low-bandgap PVSCs. The excellent performance is enabled by the use of relatively thick ($\sim$600 nm) low-bandgap mixed Sn–Pb perovskite thin films with large grains and long carrier lifetimes (up to 250 ns). When mechanically stacked with a $\sim$1.58 eV bandgap perovskite top cell, our best all-perovskite 4-terminal tandem solar cell obtains a maximum PCE of 21.2% and a steady-state efficiency of 21.0%. Our results demonstrate the feasibility of using low-bandgap mixed Sn–Pb perovskites as the bottom cell in tandem solar cells and pave the way to realize high-efficiency all-perovskite monolithic tandem solar cells.

Photovoltaic performance

Our previous work has established an effective approach to fabricate low-bandgap mixed Sn–Pb perovskite solar cells by mixing $FASnI_3$ and $MAPbI_3$ precursors with different molar ratios. We found that $(FASnI_3)_{0.6}(MAPbI_3)_{0.4}$ perovskite films exhibit a bandgap of approximately 1.25 eV and the inverted planar PVSCs with a structure of indium-doped tin oxide (ITO)/poly(3,4-ethylenedioxythiophene):polystyrene sulfonate (PEDOT:PSS)/$(FASnI_3)_{0.6}(MAPbI_3)_{0.4}$/fullerene ($C_{60}$)/2,9-dimethyl-4,7-diphenyl-1,10-phenanthroline (BCP)/Ag can achieve PCEs up to $\sim$15% (ref. 16). However, the spectral response in the IR wavelength range of 700 to 900 nm is too low, which is the critical spectral region transmitted through the top cell to the bottom cell. Analysis on the EQE suggests that the relatively low EQE in the IR wavelength range of 700 to 900 nm is primarily due to the insufficient absorption caused by the relatively thin ($\sim$400 nm) mixed Sn–Pb perovskite layers. However, simply increasing the thickness of the mixed Sn–Pb perovskite layers results only in PVSCs with decreased J_{sc}, due to their short carrier lifetime ($<$20 ns); photo-generated carriers recombine before they reach electron/hole selective contacts[10,16,17,21]. Therefore, to enhance the EQE in the IR wavelength range of 700 to 900 nm, thicker mixed Sn–Pb perovskite thin films with enhanced carrier lifetimes must be developed. We find that the carrier lifetimes of mixed Sn–Pb perovskite thin films are crucially determined by film crystallinity. Through optimization of the precursor concentration, we are now able to grow Sn–Pb perovskite thin films with thicknesses up to $\sim$1,000 nm and with carrier lifetimes longer than 250 ns. Such high-quality thick Sn–Pb perovskite absorber films enable us to fabricate efficient lower-bandgap PVSCs with EQEs of more than 70% in the IR range of 700 to 900 nm wavelength and V_{oc} up to 0.85 V.

Figure 1a shows a cross-sectional scanning electron microscopy (SEM) image of a complete PVSC, in which the $(FASnI_3)_{0.6}(MAPbI_3)_{0.4}$ absorber has an approximate thickness of 620 nm. The functionalities of each layer have been discussed in our previous works[16,29,30]. Figure 1b shows the current density–voltage (J–V) curves of our best-performing low-bandgap PVSC using an approximately 620-nm-thick $(FASnI_3)_{0.6}(MAPbI_3)_{0.4}$ absorber layer. This cell shows a PCE of 17.6 (17.5)% with a V_{oc} of 0.853 (0.854) V, a J_{sc} of 28.5 (28.7) mA cm^{-2}, and a fill factor (FF) of 72.5 (71.4)% when measured under forward (reverse) voltage scan, exhibiting a negligible degree of J–V hysteresis, the reasons for which will be discussed later. To verify our device performance, one cell was sent to the accredited Technology and Application Center PV Lab of Newport Corporation for efficiency certification, confirming a PCE of 17.01% (Supplementary Fig. 1). To the best of our knowledge, this PCE is so far the highest certified efficiency for low-bandgap

PVSCs ($\sim$1.25 eV). Furthermore, the small degree of J–V hysteresis of our devices has been verified by the J–V measurements under forward and reverse scans with different scan rates, as shown in Supplementary Table 1. The PCEs of our cells do not significantly depend on the scan rate and direction.

More importantly, our new low-bandgap PVSCs show significantly enhanced EQE in the IR wavelength range of 700 to 900 nm, which is critical for the bottom cells to be used for tandem device applications. Figure 1c shows the EQE spectrum of our best-performing cell and its corresponding integrated J_{sc} over a 100 mW cm^{-2} AM1.5G solar spectrum is 28.6 mA cm^{-2}, consistent with the J_{sc} extracted from the J–V measurements. In agreement with our previous work[16], the EQE spectrum indicates a spectral response onset of approximately 1,030 nm. It is important to note that the 620-nm-thick $(FASnI_3)_{0.6}(MAPbI_3)_{0.4}$ absorber device shows over 70% EQEs in the IR wavelength range up to 900 nm. This spectral response surpasses significantly that of all low-bandgap PVSCs reported in the literature to date, including our previous PVSCs with 15% PCE[10,13,17,20,21]. Figure 1d shows the steady-state photocurrent of approximately 25.5 mA cm^{-2} measured at a constant voltage bias of 0.667 V for 100 s under a 100 mW cm^{-2} AM1.5G illumination, generating a stabilized output power of $\sim$17.0%, which supports the PCE obtained from the J–V measurements.

We have fabricated 35 devices using 620-nm-thick $(FASnI_3)_{0.6}(MAPbI_3)_{0.4}$ absorber layers in several batches. Figure 1e shows the PCE histogram, implying that our cells have very good reproducibility. These devices achieve an average PCE of 17.2 $\pm$ 0.2% with an average V_{oc} of 0.831 $\pm$ 0.010 V, an average J_{sc} of 28.6 $\pm$ 0.1 mA cm^{-2}, and an average FF of 72.5 $\pm$ 1.1% measured under forward scan. The performance summary of PVSCs with varying thickness of $(FASnI_3)_{0.6}(MAPbI_3)_{0.4}$ absorber layers is shown in Supplementary Fig. 2 and Supplementary Table 2. It is seen that J_{sc} increases as the thickness increases from 400 to 1,010 nm. However, V_{oc} and FF firstly increase as the thickness increases, reach peak values at a thickness of 620 nm, and then decrease with further increase of the thickness. The overall PCE reaches a peak value at thickness of 620 nm, suggesting the device performance is optimal with this thick $(FASnI_3)_{0.6}(MAPbI_3)_{0.4}$ absorber. Our encapsulated cells with 620-nm-thick $(FASnI_3)_{0.6}(MAPbI_3)_{0.4}$ absorber retained 94% of their initial efficiencies after 33 days as shown in Supplementary Fig. 3, implying the reasonable stability of mixed Sn–Pb PVSCs.

Characterization of perovskites with varying thickness

We find that the carrier lifetimes of mixed Sn–Pb perovskite thin films depend critically on their grain sizes and crystallinity, with larger grains and/or higher crystallinity leading to longer carrier lifetimes. Figure 2a–d shows the top-view SEM images of $(FASnI_3)_{0.6}(MAPbI_3)_{0.4}$ films with different thickness of 400, 510, 620 and 1,010 nm, respectively. All perovskite films are compact and pinhole-free, which is highly desirable for efficient PVSC fabrication, especially in Sn-based PVSCs[13,15,30–33]. The 400-nm-thick perovskite film (Fig. 2a) shows similar morphology as reported in our previous work[16], giving an average grain size of 300–400 nm. This film was used as a control in this work. Figure 2a–d shows clearly that the average grain size increases as the thickness increases. Figure 2e–h shows the cross-sectional SEM images of completed PVSCs with varying thickness of $(FASnI_3)_{0.6}(MAPbI_3)_{0.4}$ layers deposited with identical conditions of absorbers shown in Fig. 2a–d, implying the perovskite layers shown in Fig. 2a and e; b and f; c and g; and d and h should have the same thickness, respectively. It is seen that the grain size for each thickness is comparable to the film thickness. Assuming that grain boundaries may cause carrier scattering and recombination, thicker perovskite films composed of large grains are desirable for fabricating $(FASnI_3)_{0.6}(MAPbI_3)_{0.4}$ PVSCs to achieve enhanced EQEs in the IR wavelength region[34].
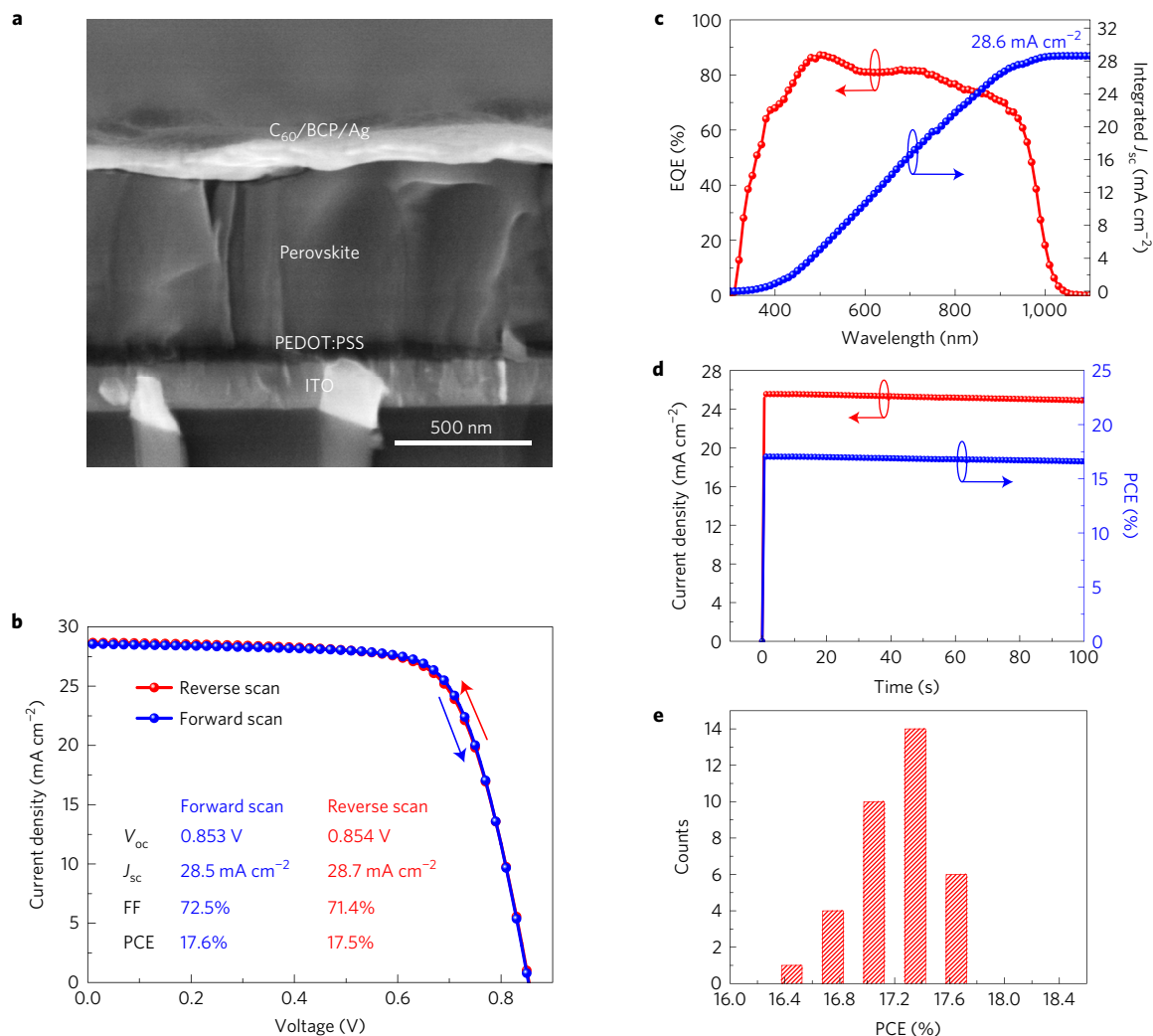
Figure 1 | Device architecture schematic and performance. a, Cross-sectional SEM image of a PVSC with a 620 nm $(FASnI_3)_{0.6}(MAPbI_3)_{0.4}$ absorber. The scale bar is 500 nm. **b**, J–V curves under 100 mW cm^{-2} AM1.5 G illumination measured under reverse and forward scans as indicated by two colours of arrows. **c**, EQE spectrum and integrated J_{sc}. The integrated J_{sc} over a 100 mW cm^{-2} AM1.5G solar spectrum is 28.6 mA cm^{-2}. **d**, Steady-state photocurrent and PCE at a constant bias of 0.667 V, of our best-performing lower-bandgap solar cell using 620 nm $(FASnI_3)_{0.6}(MAPbI_3)_{0.4}$ as absorbers. The arrows indicate the corresponding steady-state photocurrent of approximately 25.5 mA cm^{-2} and steady-state efficiency of ~17.0% under a 100 mW cm^{-2} AM1.5G illumination. **e**, Histograms of PCEs measured for 35 cells using 620 nm $(FASnI_3)_{0.6}(MAPbI_3)_{0.4}$ absorbers.

Optical absorption spectra and X-ray diffraction (XRD) measurements show that $(FASnI_3)_{0.6}(MAPbI_3)_{0.4}$ absorbers with different thickness exhibit the same optical properties and crystallographic orientation of perovskite grains. As shown in Fig. 2i, the absorption intensity increases as the film thickness increases. However, the absorption onsets of all perovskite films are identical, indicating that the bandgaps of all perovskites are the same. The variation in film thickness does not change the bandgap of ~1.25 eV for the $(FASnI_3)_{0.6}(MAPbI_3)_{0.4}$ perovskite films, which is determined by fitting the $(\alpha h\nu)^2 - E$ plot of a perovskite film as shown in Supplementary Fig. 4. The atomic ratio of Sn/Pb of our $(FASnI_3)_{0.6}(MAPbI_3)_{0.4}$ perovskite was confirmed to be 8.97:6.13 by energy-dispersive X-ray spectroscopy and also X-ray photoelectron spectroscopy in our previous work[16], which is very close to 60:40 as expected. XRD patterns taken from $(FASnI_3)_{0.6}(MAPbI_3)_{0.4}$ films with different thickness show very similar features (Fig. 2j), suggesting that the thickness variation does not affect grain orientation of $(FASnI_3)_{0.6}(MAPbI_3)_{0.4}$ perovskite films. All XRD patterns show strong (110) and (220) reflection peaks, indicating a highly preferred orientation. The full-width at half-maximum (FWHM) values of the (110) peak from XRD

patterns of $(FASnI_3)_{0.6}(MAPbI_3)_{0.4}$ films with thicknesses of 400, 510, 620 and 1,010 nm are 0.100° ± 0.003°, 0.091° ± 0.001°, 0.088° ± 0.001° and 0.093° ± 0.001°, respectively (Supplementary Fig. 5). This trend of FWHM values indicates that the 620-nm-thick perovskite film has the highest crystallinity, since SEM images show that the grain size increases as the thickness increases.

Time-resolved photoluminescence (TRPL) measurements (Fig. 2k) show a trend similar to that of the FWHM values of the (110) peak. The 400-nm-thick $(FASnI_3)_{0.6}(MAPbI_3)_{0.4}$ perovskite film shows a mean photo-generated carrier lifetime of 15 ns, comparable to that in our previously reported perovskite film with a similar thickness[16]. The carrier lifetime is increased to 96 ns when the film thickness is increased to 510 nm. The carrier lifetime is substantially increased to 255 ns when the film thickness is further increased to 620 nm. Such a remarkably long carrier lifetime is even comparable to that of reported pure Pb perovskites[5]. The increase in carrier lifetime is consistent with the increase of film crystallinity as revealed by the FWHM values of the (110) peak as shown in Supplementary Fig. 5. When the film thickness is increased to 1,010 nm, the carrier lifetime decreases slightly to 226 ns, although the average grain size is larger than that of the 620-nm-thick
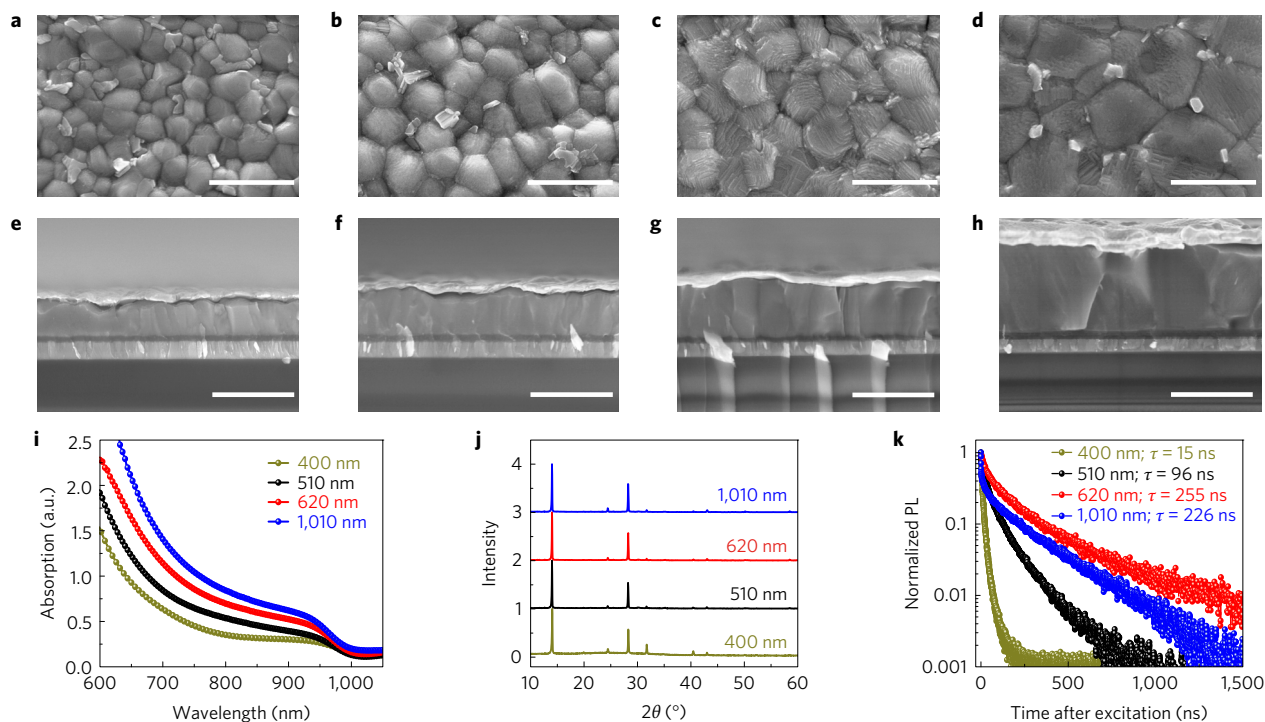
Figure 2 | Characterization of (FASnI₃)₀.₆(MAPbI₃)₀.₄ perovskite films. a–d, Top-view SEM images of $(FASnI_3)_{0.6}(MAPbI_3)_{0.4}$ perovskite films (**a**, 400 nm; **b**, 510 nm; **c**, 620 nm; and **d**, 1,010 nm) deposited on PEDOT:PSS-coated ITO substrates. **e–h**, Cross-sectional SEM images of our completed devices with different thickness of $(FASnI_3)_{0.6}(MAPbI_3)_{0.4}$ as absorbers (**e**, 400 nm; **f**, 510 nm; **g**, 620 nm; and **h**, 1,010 nm). The layer stack in each image is identical to the layer stack in Fig. 1a, consisting of ITO, PEDOT:PSS, $(FASnI_3)_{0.6}(MAPbI_3)_{0.4}$ absorber, and C_{60}/BCP/Ag from bottom to top. **i**, Absorption spectra of $(FASnI_3)_{0.6}(MAPbI_3)_{0.4}$ perovskite films with different thickness. **j**, XRD patterns of $(FASnI_3)_{0.6}(MAPbI_3)_{0.4}$ perovskite films with different thickness. **k**, Normalized time-resolved photoluminescence decay of $(FASnI_3)_{0.6}(MAPbI_3)_{0.4}$ perovskite films with different thickness. The carrier lifetime in **k** for the biexponential fit is calculated by the weighted average method as described in more detail in the Methods and Supplementary Table 3. The scale bar in images **a–h** is 1 μm.
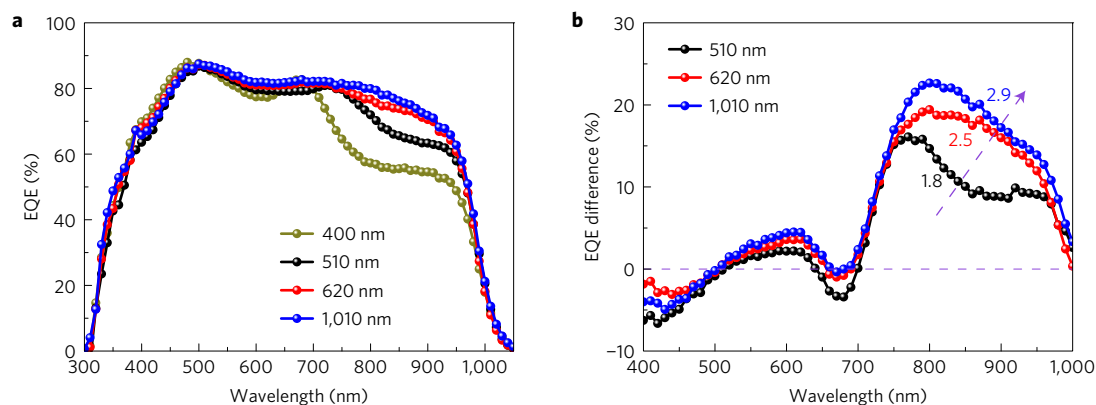

Figure 3 | EQE spectra of (FASnI₃)₀.₆(MAPbI₃)₀.₄ PVSCs. a, EQE spectra of our PVSCs with different thickness of $(FASnI_3)_{0.6}(MAPbI_3)_{0.4}$ absorbers (400, 510, 620 and 1,010 nm). **b**, EQE variation of other PVSCs with thick $(FASnI_3)_{0.6}(MAPbI_3)_{0.4}$ absorbers (510, 620 and 1,010 nm) versus the thinnest one (400 nm). Increases in integrated device J_{sc} values compared with the thinnest PVSC J_{sc} are indicated next to different curves by the dashed arrow.

film. Therefore, the decreased carrier lifetime is attributed to the decreased crystallinity as evidenced by the FWHM values of the (110) peak. Our TRPL results reveal that thick low-bandgap mixed Sn–Pb perovskite films with long carrier lifetimes and improved crystallinity were successfully synthesized. A longer charge carrier lifetime is required to achieve high-performance PVSCs with thicker absorbers, because photo-generated carriers must, on average, survive to travel a longer distance before they are collected[34]. The measured carrier lifetimes explain very well the device performance of $(FASnI_3)_{0.6}(MAPbI_3)_{0.4}$ PVSCs with different thickness as shown in Supplementary Fig. 2 and

Supplementary Table 2. A longer carrier lifetime indicates a lower non-radiative recombination rate, which should lead to a higher V_{oc} and FF. The highest V_{oc} and FF are achieved for the PVSC with a 620-nm-thick absorber, which also exhibits the longest carrier lifetime. As the absorber layer thickness increases, the J_{sc} is significantly increased.

To evaluate the electronic quality of the mixed Sn–Pb perovskite films with different thicknesses, we calculated the Urbach energies using the method described in the literature (Supplementary Fig. 6)[35–37]. The calculated Urbach energies are 20.6, 19.2, 18.8 and 20.8 meV for 400-, 510-, 620- and 1,010-nm-thick
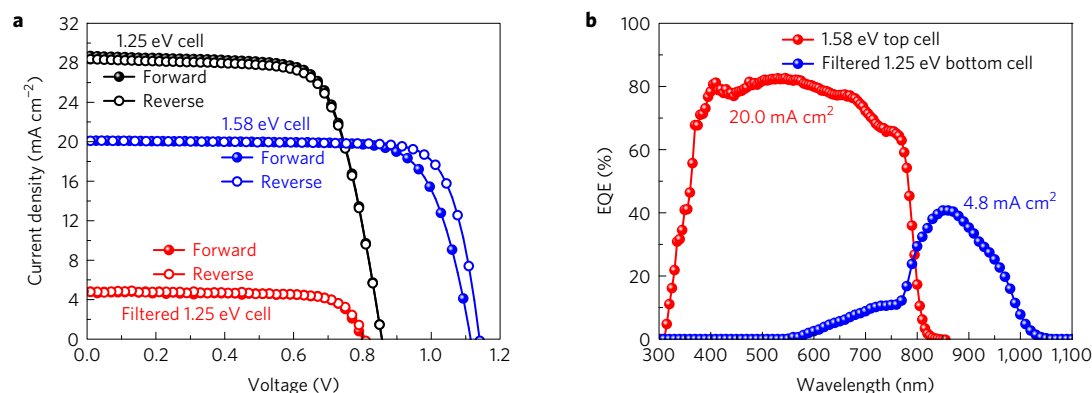
Figure 4 | Characterization of the all-perovskite 4-terminal tandem cell. a, *J–V* curves of the semi-transparent wide-bandgap (1.58 eV) PVSC under glass/FTO illumination and the low-bandgap (1.25 eV) PVSC with and without the semi-transparent wide-bandgap PVSC optical filter. **b**, EQE spectra of semi-transparent wide-bandgap (1.58 eV) PVSC top cell and filtered low-bandgap (1.25 eV) PVSC bottom cell. The integrated J_{sc} over a 100 mW cm^{-2} AM1.5G solar spectrum for the 1.58 eV top cell and the filtered 1.25 eV bottom cell is 20.0 and 4.8 mA cm^{-2}, respectively.

Table 1 | Performance of single and tandem PVSCs.

Cells		V_{oc} (V)	J_{sc} (mA cm^{-2})	FF (%)	PCE (%)	SSE
1.58 eV cell	Forward	1.114	20.1	76.4	17.1	17.9
	Reverse	1.141	20.1	80.0	18.3	
1.25 eV cell	Forward	0.857	28.7	71.3	17.5	
	Reverse	0.856	28.3	71.7	17.4	
Filtered 1.25 eV cell	Forward	0.800	4.8	76.3	2.9	3.1
	Reverse	0.808	4.8	74.4	2.9	
4-terminal tandem cell	Forward				20.0	21.0
	Reverse				21.2	

A summary of the main performance metrics of the semi-transparent wide-bandgap (1.58 eV) perovskite top cell, the low-bandgap (1.25 eV) perovskite bottom cell, the filtered low-bandgap (1.25 eV) perovskite bottom cell, and the summated all-perovskite 4-terminal tandem cell. SSE, steady-state efficiency. The defined areas of the 1.58 eV cell and the 1.25 eV cell are 0.10 and 0.105 cm^2, respectively.

(FASnI$_3$)$_{0.6}$(MAPbI$_3$)$_{0.4}$ perovskite thin films, respectively. The trend of the Urbach energy as a function of film thickness correlates with the trend of carrier lifetimes determined by TRPL and crystallinity evidenced by FWHM values. A smaller Urbach energy should correspond to a lower density of trap states. The variations in trap density should impact device performance[37–39].

The small degree of *J–V* hysteresis of our (FASnI$_3$)$_{0.6}$(MAPbI$_3$)$_{0.4}$ PVSCs is attributed to the pinhole-free compact perovskite layers, large grain sizes, and the use of C$_{60}$ as the passivation layer at the perovskite/electron-selective layer (ESL) interfaces. The thermally evaporated C$_{60}$/BCP ESLs provide complete coverage of the perovskite layer although the surface roughness is high[16,29,30,40,41].

EQE enhancement in the IR range

Figure 3a shows the representative EQE spectra of PVSCs with different thicknesses of (FASnI$_3$)$_{0.6}$(MAPbI$_3$)$_{0.4}$ absorber layers. Their EQE-integrated J_{sc} values are 26.2, 28.1, 28.7 and 29.3 mA cm^{-2} for PVSCs with 400-, 510-, 620- and 1,010-nm-thick (FASnI$_3$)$_{0.6}$(MAPbI$_3$)$_{0.4}$ absorbers, respectively. It is seen that the EQE values for PVSCs with 510-, 620- and 1,010-nm-thick (FASnI$_3$)$_{0.6}$(MAPbI$_3$)$_{0.4}$ absorbers increase in the wavelength range from 700 to 1,000 nm as compared with that of the cell using a 400-nm-thick absorber. To view the enhancement more clearly, we calculated the EQE difference with respect to that of a 400-nm-thick control cell. As shown in Fig. 3b, the EQE enhancements occur in the wavelength range of 700 to 1,000 nm. The 510-, 620- and 1,010-nm-thick (FASnI$_3$)$_{0.6}$(MAPbI$_3$)$_{0.4}$ PVSCs gain an integrated J_{sc} of 1.8, 2.5 and 2.9 mA cm^{-2} in the range of 700–1,000 nm, respectively, as compared with the 400-nm-thick control device.

These J_{sc} gains in the IR range are of great significance for the bottom-cell performance.

All-perovskite 4-terminal tandem PVSCs

We mechanically stacked a (FASnI$_3$)$_{0.6}$(MAPbI$_3$)$_{0.4}$ bottom cell with a semi-transparent wide-bandgap (~1.58 eV) FA$_{0.3}$MA$_{0.7}$PbI$_3$ top cell to form an all-perovskite 4-terminal tandem cell. The corresponding *J–V* curves and PV parameter summary are shown in Fig. 4a and Table 1. The integrated J_{sc} from the measured EQE (Fig. 4b) of the filtered bottom cell is 20.0 mA cm^{-2}, consistent with the J_{sc} obtained from the *J–V* curve. The 4-terminal tandem cell obtains a PCE of 21.2 (20.0)%, which is higher than the semi-transparent top cell, 18.3 (17.1)%, and filtered bottom cell, 2.9 (2.9)%, measured under the reverse (forward) voltage scan. The corresponding steady-state efficiency is 17.9% for the top cell and 3.1% for the bottom cell filtered by the top cell sample at a region with large back contact (Supplementary Fig. 7). The top cell has a regular cell configuration of glass/FTO/SnO$_2$/fullerene-self-assembly monolayer (C$_{60}$-SAM)/FA$_{0.3}$MA$_{0.7}$PbI$_3$/Spiro-MeTAD/MoO$_x$(10 nm)/Au(8.5 nm)/MoO$_x$(10 nm), whose transmittance spectrum is shown in Supplementary Fig. 8. The first 10 nm MoO$_x$ layer acts as both a hole buffer layer and a wetting layer for Au deposition[42–44]. The Volmer–Weber growth mechanism for depositing metals such as Au and Ag results in the formation of metal islands[23,42]. A MoO$_x$ wetting layer changes the growth mechanism and allows the deposition of ultrathin Au without the formation of islands, which is desirable for enhancing transparency and reducing sheet resistance[43]. The second MoO$_x$ layer is employed to form a dielectric–metal–dielectric stack to tune the light dispersion

characteristics of the semi-transparent electrode (Supplementary Fig. 9), further enhancing the transparency so that more light can pass through the top cell[43]. The reflectance spectra of MoO_x/Au and $MoO_x/Au/MoO_x$ thin films are also shown in Supplementary Fig. 9. The sheet resistances for MoO_x/Au and $MoO_x/Au/MoO_x$ are 12.2 and 11.8 Ω per square, respectively, indicating that the capping layer of 10 nm MoO_x does not significantly change the sheet resistance. As seen in Supplementary Fig. 9, the ultrathin Au layer still exhibits significant absorption in the IR wavelength range, even with the use of dielectric–metal–dielectric structure. Furthermore, the ultrathin Au electrode also limits the FF of the top cell. Therefore, the PCE of our 4-terminal tandem cell is still limited by the performance of the top cell, which uses a perovskite absorber with a bandgap not wide enough to optimally match with the bottom cell and a semi-transparent metal electrode.

Conclusion

We have demonstrated efficient low-bandgap (~1.25 eV) PVSCs with the highest PCE to date, over 17.6%, and a certified PCE of 17.01%. Importantly, our low-bandgap cells achieved J_{sc} values up to 29 mA cm^{-2} with EQEs of over 70% in the IR range from 700 to 900 nm and V_{oc} of up to 0.850 V, which is critical for bottom-cell applications in tandem cells. Such high-performance low-bandgap PVSCs were enabled by our thick perovskite absorber layers, which simultaneously achieve large grains/high crystallinity and very long carrier lifetimes. When mechanically stacked with a ~18% efficiency semi-transparent $FA_{0.3}MA_{0.7}PbI_3$ top cell, our all-perovskite 4-terminal tandem cell delivered an approximately 21% PCE, demonstrating the feasibility of fabricating efficient all-perovskite tandem solar cells.

Methods

Low-bandgap perovskite film preparation. The $(FASnI_3)_{0.6}(MAPbI_3)_{0.4}$ precursor solution was obtained by mixing stoichiometric amounts of $FASnI_3$ and $MAPbI_3$ perovskite precursors in mixed N,N-dimethylmethanamide (DMF)/dimethyl sulfoxide (DMSO). More details can be found in the Supplementary Methods. Different thicknesses of the $(FASnI_3)_{0.6}(MAPbI_3)_{0.4}$ layers were realized by varying the precursor concentration, leading to the approximate thickness of 400, 510, 620 and 1,010 nm. The $(FASnI_3)_{0.6}(MAPbI_3)_{0.4}$ precursors were spin-coated onto ITO/PEDOT:PSS at 5,000 r.p.m. for 60 s. Diethyl ether was applied to conduct solvent engineering. All perovskite films were annealed at 100 °C for 7 min. The samples for SEM and UV–Vis measurements were prepared on ITO/PEDOT:PSS and glass/PEDOT:PSS. The samples for TRPL were deposited on bare glass and covered by a 30-nm-thick film of poly(methyl methacrylate) (PMMA).

Wide-bandgap perovskite film preparation. For 1.58 eV $FA_{0.3}MA_{0.7}PbI_3$ perovskite, the precursor solution with 45 wt% concentration was prepared by dissolving PbI_2, MAI, FAI and $Pb(SCN)_2$ (molar ratio = 1:0.7:0.3:0.02) in a mixed DMF/DMSO (volume ratio = 9:1). The perovskite layer was fabricated by spin-coating 70 μl precursor solution on the substrate followed by quickly dripping 0.75 ml diethyl ether on the film. The resulting film was then annealed at 100 °C for 5 min.

Device fabrication. For low-bandgap (1.25 eV) bottom cells, PEDOT:PSS films were coated on the pre-patterned and cleaned ITO substrates at 4,000 r.p.m. for 50 s and then dried at 175 °C for 30 min. The $(FASnI_3)_{0.6}(MAPbI_3)_{0.4}$ perovskite films were deposited by spin-coating onto PEDOT:PSS film at 5,000 r.p.m. for 60 s and annealed at 100 °C for 7 min. Finally, C_{60} (20 nm)/BCP(5 nm)/Ag(75 nm) were sequentially deposited by thermal evaporation to complete the fabrication. Devices were encapsulated with cover glass and UV-curable epoxy. More details can be found in the Supplementary Methods.

For 1.58 eV semi-transparent top cells, the SnO_2 ESLs were deposited onto pre-patterned and cleaned FTO substrates by plasma-enhanced atomic layer deposition (Ensure Scientific Group AutoALD-PE V2.0) following the process and treatment described in our earlier work[2]. A C_{60}-SAM layer passivating the ESLs, $FA_{0.3}MA_{0.7}PbI_3$ perovskite films, and spiro-OMeTAD as hole-selective layers were deposited following a previously reported method[2]. Finally, 10 nm MoO_x, 8.5 nm Au and 10 nm MoO_x were thermally evaporated sequentially through a patterned mask onto the hole-selective layers. The active area of each device ranged from 0.085 to 0.12 cm^2 and was defined by a mask. More details can be found in the Supplementary Methods.

Film and device characterization. High-resolution field emission top-view and cross-sectional SEM images of $(FASnI_3)_{0.6}(MAPbI_3)_{0.4}$ perovskite films with the thickness of 400, 510, 620 and 1,010 nm were taken with Hitachi S-4800. The crystal structure of different thick $(FASnI_3)_{0.6}(MAPbI_3)_{0.4}$ films was examined by X-ray diffraction (RigakuUltima III) with Cu Kα radiation under operation conditions of 40 kV and 44 mA excitation. The absorption spectra were measured by UV–Vis spectrophotometer (PerkinElmer Lambda 1050). All layer thicknesses were determined using a Dektak surface profiler and cross-sectional SEM images. TRPL measurements were conducted similarly as described in our earlier work[2,16]. Photoluminescence decay curves were biexponential in nature and fitted by iterative re-convolution with the measured system response function. Mean photo-generated carrier lifetimes (see Supplementary Table 3) for the biexponential fit are calculated by the weighted average method[2]. The Urbach energy was measured on the basis of the equation of $\eta(h\nu) = \eta_0 e^{(h\nu - E_0)/E_{Urbach}}$, where $\eta(h\nu)$ is the EQE value and E_{Urbach} is the Urbach energy[37]. J–V curves were measured in air under 100 mW cm^{-2} AM1.5G solar irradiation (PV Measurements) with a Keithley 2400 Source Meter. The incident light was controlled by a shutter. The light intensity for J–V measurements was calibrated by a standard Si solar cell and our perovskite solar cells certified by Newport. The steady-state efficiencies were obtained by tracking the maximum output power point. EQE spectra were performed from 300 to 1,150 nm on a QE system (PV Measurements, model IVQE8-C QE system without bias voltage). All characterizations and measurements were performed in the ambient. One of our $(FASnI_3)_{0.6}(MAPbI_3)_{0.4}$ devices was sent to an accredited PV laboratory of Newport Corporation for PCE certification. More details can be found in the Supplementary Methods.

4-terminal tandem cell measurements. The J–V curves of semi-transparent top cells were measured in air under 100 mW cm^{-2} AM1.5G solar irradiation, and their steady-state efficiency was obtained at the maximum power point for over a period of 100 s. EQE spectra were performed on a QE system. The top cell with an active area of 0.10 cm^2 as defined by the mask and the bottom cell with a masked area of 0.105 cm^2 are measured, separately. Each semi-transparent wide-bandgap top-cell sample consists of multiple subcells with small and large active areas as defined by the areas of the metal electrodes. The small subcells have similar active areas as the bottom cells and are used for J–V measurements. The large subcells are used to filter the bottom cells for easy cell alignment. The J–V curves, steady-state efficiency, and EQE spectrum of 1.25 eV bottom cells were taken by putting such a semi-transparent wide-bandgap top cell with a large active area on top as a filter.

Data availability. The data that support the findings of this study are available from the corresponding author on request.

References

1. McMeekin, D. P. et al. A mixed-cation lead mixed-halide perovskite absorber for tandem solar cells. Science **351**, 151–155 (2016).
2. Wang, C. et al. Low-temperature plasma-enhanced atomic layer deposition of tin oxide electron selective layers for highly efficient planar perovskite solar cells. J. Mater. Chem. A **4**, 12080–12087 (2016).
3. Yin, W.-J., Yang, J.-H., Kang, J., Yan, Y. & Wei, S.-H. Halide perovskite materials for solar cells: a theoretical review. J. Mater. Chem. A **3**, 8926–8942 (2015).
4. Yin, W.-J., Shi, T. & Yan, Y. Unique properties of halide perovskites as possible origins of the superior solar cell performance. Adv. Mater. **26**, 4653–4658 (2014).
5. Stranks, S. D. et al. Electron-hole diffusion lengths exceeding 1 micrometer in an organometal trihalide perovskite absorber. Science **342**, 341–344 (2013).
6. Kojima, A., Teshima, K., Shirai, Y. & Miyasaka, T. Organometal halide perovskites as visible-light sensitizers for photovoltaic cells. J. Am. Chem. Soc. **131**, 6050–6051 (2009).
7. Bi, D. et al. Polymer-templated nucleation and crystal growth of perovskite films for solar cells with efficiency greater than 21%. Nat. Energy **1**, 16142 (2016).
8. Yang, W. S. et al. High-performance photovoltaic perovskite layers fabricated through intramolecular exchange. Science **348**, 1234–1237 (2015).
9. Kim, H.-S. et al. Lead iodide perovskite sensitized all-solid-state submicron thin film mesoscopic solar cell with efficiency exceeding 9%. Sci. Rep. **2**, 591 (2012).
10. Eperon, G. E. et al. Perovskite-perovskite tandem photovoltaics with optimized bandgaps. Science **354**, 861–865 (2016).
11. Yu, Z., Leilaeioun, M. & Holman, Z. Selecting tandem partners for silicon solar cells. Nat. Energy **1**, 16137 (2016).
12. Meillaud, F., Shah, A., Droz, C., Vallat-Sauvain, E. & Miazza, C. Efficiency limits for single-junction and tandem solar cells. Sol. Energy Mater. Sol. Cells **90**, 2952–2959 (2006).

13. Hao, F., Stoumpos, C. C., Chang, R. P. H. & Kanatzidis, M. G. Anomalous band gap behavior in mixed Sn and Pb perovskites enables broadening of absorption spectrum in solar cells. *J. Am. Chem. Soc.* **136**, 8094–8099 (2014).

14. Im, J., Stoumpos, C. C., Jin, H., Freeman, A. J. & Kanatzidis, M. G. Antagonism between spin–orbit coupling and steric effects causes anomalous band gap evolution in the perovskite photovoltaic materials $CH_3NH_3Sn_{1-x}Pb_xI_3$. *J. Phys. Chem. Lett.* **6**, 3503–3509 (2015).

15. Stoumpos, C. C., Malliakas, C. D. & Kanatzidis, M. G. Semiconducting tin and lead iodide perovskites with organic cations: phase transitions, high mobilities, and near-infrared photoluminescent properties. *Inorg. Chem.* **52**, 9019–9038 (2013).

16. Liao, W. *et al.* Fabrication of efficient low-bandgap perovskite solar cells by combining formamidinium tin iodide with methylammonium lead iodide. *J. Am. Chem. Soc.* **138**, 12360–12363 (2016).

17. Ogomi, Y. *et al.* $CH_3NH_3Sn_xPb_{(1-x)}I_3$ perovskite solar cells covering up to 1060 nm. *J. Phys. Chem. Lett.* **5**, 1004–1011 (2014).

18. Anaya, M. *et al.* Optical analysis of $CH_3NH_3Sn_xPb_{1-x}I_3$ absorbers: a roadmap for perovskite-on-perovskite tandem solar cells. *J. Mater. Chem. A* **4**, 11214–11221 (2016).

19. Zuo, F. *et al.* Binary-metal perovskites toward high-performance planar-heterojunction hybrid solar cells. *Adv. Mater.* **26**, 6454–6460 (2014).

20. Yang, Z. *et al.* Stable low-bandgap Pb–Sn binary perovskites for tandem solar cells. *Adv. Mater.* **28**, 8990–8997 (2016).

21. Li, Y. *et al.* 50% Sn-based planar perovskite solar cell with power conversion efficiency up to 13.6%. *Adv. Energy Mater.* **6**, 1601353 (2016).

22. Bailie, C. D. *et al.* Semi-transparent perovskite solar cells for tandems with silicon and CIGS. *Energy Environ. Sci.* **8**, 956–963 (2015).

23. Chen, B. *et al.* Efficient semitransparent perovskite solar cells for 23.0%-efficiency perovskite/silicon four-terminal tandem cells. *Adv. Energy Mater.* **6**, 1601128 (2016).

24. Werner, J. *et al.* Efficient near-infrared-transparent perovskite solar cells enabling direct comparison of 4-terminal and monolithic perovskite/silicon tandem cells. *ACS Energy Lett.* **1**, 474–480 (2016).

25. Fu, F. *et al.* Low-temperature-processed efficient semi-transparent planar perovskite solar cells for bifacial and tandem applications. *Nat. Commun.* **6**, 8932 (2015).

26. Fu, F. *et al.* High-efficiency inverted semi-transparent planar perovskite solar cells in substrate configuration. *Nat. Energy* **2**, 16190 (2016).

27. Kranz, L. *et al.* High-efficiency polycrystalline thin film tandem solar cells. *J. Phys. Chem. Lett.* **6**, 2676–2681 (2015).

28. Liu, J., Lu, S., Zhu, L., Li, X. & Choy, W. C. H. Perovskite-organic hybrid tandem solar cells using a nanostructured perovskite layer as the light window and a PFN/doped-MoO3/MoO3 multilayer as the interconnecting layer. *Nanoscale* **8**, 3638–3646 (2016).

29. Zhao, D. *et al.* High-efficiency solution-processed planar perovskite solar cells with a polymer hole transport layer. *Adv. Energy Mater.* **5**, 1401855 (2015).

30. Liao, W. *et al.* Lead-free inverted planar formamidinium tin triiodide perovskite solar cells achieving power conversion efficiencies up to 6.22%. *Adv. Mater.* **28**, 9333–9340 (2016).

31. Zhao, D. *et al.* Annealing-free efficient vacuum-deposited planar perovskite solar cells with evaporated fullerenes as electron-selective layers. *Nano Energy* **19**, 88–97 (2016).

32. Lee, S. J. *et al.* Fabrication of efficient formamidinium tin iodide perovskite solar cells through SnF2–pyrazine complex. *J. Am. Chem. Soc.* **138**, 3974–3977 (2016).

33. Chung, I., Lee, B., He, J., Chang, R. P. H. & Kanatzidis, M. G. All-solid-state dye-sensitized solar cells with high efficiency. *Nature* **485**, 486–489 (2012).

34. Xiao, Z. *et al.* Solvent annealing of perovskite-induced crystal growth for photovoltaic-device efficiency enhancement. *Adv. Mater.* **26**, 6503–6509 (2014).

35. De Wolf, S. *et al.* Organometallic halide perovskites: sharp optical absorption edge and its relation to photovoltaic performance. *J. Phys. Chem. Lett.* **5**, 1035–1039 (2014).

36. Sadhanala, A. *et al.* Preparation of single-phase films of $CH_3NH_3Pb(I_{1-x}Br_x)_3$ with sharp optical band edges. *J. Phys. Chem. Lett.* **5**, 2501–2505 (2014).

37. Wang, J. T.-W. *et al.* Efficient perovskite solar cells by metal ion doping. *Energy Environ. Sci.* **9**, 2892–2901 (2016).

38. Johnson, S. R. & Tiedje, T. Temperature dependence of the Urbach edge in GaAs. *J. Appl. Phys.* **78**, 5609–5613 (1995).

39. Zanatta, A. R. & Chambouleyron, I. Absorption edge, band tails, and disorder of amorphous semiconductors. *Phys. Rev. B* **53**, 3833–3836 (1996).

40. Shao, Y., Xiao, Z., Bi, C., Yuan, Y. & Huang, J. Origin and elimination of photocurrent hysteresis by fullerene passivation in $CH_3NH_3PbI_3$ planar heterojunction solar cells. *Nat. Commun.* **5**, 5784 (2014).

41. Shao, Y., Yuan, Y. & Huang, J. Correlation of energy disorder and open-circuit voltage in hybrid perovskite solar cells. *Nat. Energy* **1**, 15001 (2016).

42. Zhang, C. *et al.* An ultrathin, smooth, and low-loss Al-doped Ag film and its application as a transparent electrode in organic photovoltaics. *Adv. Mater.* **26**, 5696–5701 (2014).

43. Zhao, D., Zhang, C., Kim, H. & Guo, L. J. High-performance Ta2O5/Al-doped Ag electrode for resonant light harvesting in efficient organic solar cells. *Adv. Energy Mater.* **5**, 1500768 (2015).

44. Zhao, D. W. *et al.* Optimization of inverted tandem organic solar cells. *Sol. Energy Mater. Sol. Cells* **95**, 921–926 (2011).

Acknowledgements

Author contributions

D.Z. and Y.Yan conceived the project. D.Z. carried out film and device fabrication and characterization. Y.Yu and C.W. prepared wide-bandgap perovskite film and devices. Y.Yu assisted with SEM measurement. W.L. assisted in device fabrication and characterization. C.R.G., A.J.C. and L.G. helped with the characterization. N.S. and R.J.E. conducted TRPL measurements. D.Z. and Y.Yan analysed the data and wrote the manuscript. K.Z. and R.-G.X. helped with the manuscript preparation. All the authors discussed the results and commented on the manuscript. Y.Yan supervised the project.

Additional information

Competing interests

The authors declare no competing financial interests.